

Benchmark study of the recent version of the PHITS code

Yosuke Iwamoto, Tatsuhiko Sato, Shintaro Hashimoto, Tatsuhiko Ogawa, Takuya Furuta, Shin-ichiro Abe, Takeshi Kai, Norihiro Matsuda, Ryuji Hosoyamada & Koji Niita

To cite this article: Yosuke Iwamoto, Tatsuhiko Sato, Shintaro Hashimoto, Tatsuhiko Ogawa, Takuya Furuta, Shin-ichiro Abe, Takeshi Kai, Norihiro Matsuda, Ryuji Hosoyamada & Koji Niita (2017) Benchmark study of the recent version of the PHITS code, Journal of Nuclear Science and Technology, 54:5, 617-635, DOI: [10.1080/00223131.2017.1297742](https://doi.org/10.1080/00223131.2017.1297742)

To link to this article: <https://doi.org/10.1080/00223131.2017.1297742>



© 2017 The Author(s). Published by Informa UK Limited, trading as Taylor & Francis Group



[View supplementary material](#)



Published online: 20 Mar 2017.



[Submit your article to this journal](#)



Article views: 4266



[View related articles](#)



[View Crossmark data](#)



Citing articles: 35 [View citing articles](#)



Benchmark study of the recent version of the PHITS code

Yosuke Iwamoto^a, Tatsuhiko Sato^a, Shintaro Hashimoto^a, Tatsuhiko Ogawa^a, Takuya Furuta^a, Shin-ichiro Abe^a, Takeshi Kai^a, Norihiro Matsuda^a, Ryuji Hosoyamada^b and Koji Niita^b

^aJapan Atomic Energy Agency, Ibaraki, Japan; ^bResearch Organization for Information Science and Technology, Ibaraki, Japan

ABSTRACT

We performed a benchmark study for 58 cases (22 cases reported in this paper and 36 cases reported in online as supplementary materials of this paper) using the recent version (version 2.88) of the Particle and Heavy-Ion Transport code System (PHITS) in the following fields: (1) particle production cross-sections for nuclear reactions from 20 MeV to 1 GeV, (2) thick-target neutron yields and neutron shielding, (3) depth-dose distribution in water using ¹²C beam, and (4) electron and photon transportation over a wide-energy range from keV to GeV. Overall agreements were found to be sufficiently satisfactory; however, several discrepancies are observed, particularly in particle productions with energies below 100 MeV, neutron production for ⁷Li(p,n)⁷Be, and photonuclear reactions. To overcome these inaccuracies and to further improve the code, it will be necessary to incorporate a high-energy version of the evaluated nuclear data library JENDL-4.0/HE and the photonuclear data file JENDL-PD in the PHITS package.

ARTICLE HISTORY

Received 11 November 2016
Accepted 18 January 2017

KEYWORDS

PHITS; Monte Carlo calculation; benchmark; radiation shielding; nuclear reaction; electromagnetic cascade

1. Introduction

Monte Carlo codes for simulating particle transport in three-dimensional space are indispensable in various research and development fields such as nuclear technology, accelerator design, medical physics, and cosmic ray research. We have developed a general-purpose Monte Carlo Particle and Heavy-Ion Transport code System (PHITS) [1] through a collaboration between several institutes in Japan and Europe. This code uses various nuclear reaction models and data libraries in order to deal with the transport of nearly all species of particles, including neutrons, protons, heavy ions, mesons, photons, and electrons, over wide-energy ranges (10^{-5} eV–1 TeV). The benchmark calculations for a former version of PHITS (version 2.24) [2,3] were performed for accelerator shielding [4] and spallation reactions using protons [5]. In the past five years, PHITS was upgraded so as to incorporate the Liege Intranuclear Cascade model INCL4.6 [6], the algorithm and database of Electron Gamma Shower version 5 (EGS5) [7], a photonuclear reaction model [8], and the improvement of the quantum molecular dynamics model JQMD [9,10]. Although the latest version of PHITS (version 2.88) that includes these upgrades has been widely used in various research and development fields, a comprehensive comparison between experimental data and simulation results has not yet been conducted. To validate the reliability of the PHITS simulations, we conducted a comprehensive benchmark study for 58 cases using the physics models recommended for use in PHITS 2.88. For benchmark cases,

we selected target materials widely used in research and development fields of nuclear engineering such as accelerator design. As for the projectiles, we selected protons and heavy-ions with energies above 1 MeV/u and neutrons with energies above 20 MeV for validating the nuclear reaction models in PHITS, and electrons and photons for validating the EGS5 algorithm in PHITS. Note that benchmark calculations for neutrons with energies below 20 MeV are beyond the scope of this study because they have already been extensively verified [11].

This paper is organized as follows. In Section 2, we summarize the physics models used in the benchmark study. Sections 3–6 show the results for 22 cases chosen from the 58 benchmark calculations studied, and these were in the following fields: particle production cross-sections for proton and heavy-ion incident reactions (9 cases), thick-target neutron yields and neutron transport in a shielding material (5 cases), depth-dose distribution for radiotherapy using a ¹²C beam (1 case), and electromagnetic cascade for medical applications using photons and electrons (7 cases). All benchmarking results performed in this paper can be found online as supplementary materials. Finally, summaries are drawn up in Section 7.

2. Overview of the physics models used in the benchmark study

Figure 1 summarizes the physics models for simulating nuclear and atomic collisions that are recommended for use in PHITS 2.88. The intranuclear

CONTACT Yosuke Iwamoto iwamoto.yosuke@jaea.go.jp

Supplemental data for this article can be accessed at: <http://dx.doi.org/10.1080/00223131.2017.1297742>.

© 2017 The Author(s). Published by Informa UK Limited, trading as Taylor & Francis Group

This is an Open Access article distributed under the terms of the Creative Commons Attribution-NonCommercial-NoDerivatives License (<http://creativecommons.org/licenses/by-nc-nd/4.0/>), which permits non-commercial re-use, distribution, and reproduction in any medium, provided the original work is properly cited, and is not altered, transformed, or built upon in any way.

	Neutron	Proton, Pion (other hadrons)	Nucleus	Muon	e^- / e^+	Photon
	1 TeV		1 TeV/u			1 TeV
High	Intra-nuclear cascade (JAM) + Evaporation (GEM) 3.0 GeV		Quantum Molecular Dynamics (JQMD) + Evaporation (GEM)	Virtual Photo- Nuclear JAM/ JQMD + GEM	Electro magnetic cascade EGS5	Electro magnetic cascade EGS5
↑	Intra-nuclear cascade (INCL4.6) + Evaporation (GEM)		d t ^3He α 10 MeV/n	200 MeV		Photo- Nuclear JAM/ QMD + GEM + JENDL
Energy	20 MeV					
↓	Nuclear Data Library (JENDL-4.0)	1 MeV	Ionization ATIMA		1 keV	2 MeV
Low	10 ⁻⁵ eV	1 keV			1 keV	1 keV

Figure 1. Physics models recommended for use in Particle and Heavy-Ion Transport code System (PHITS) 2.88 for simulating nuclear and atomic collisions.

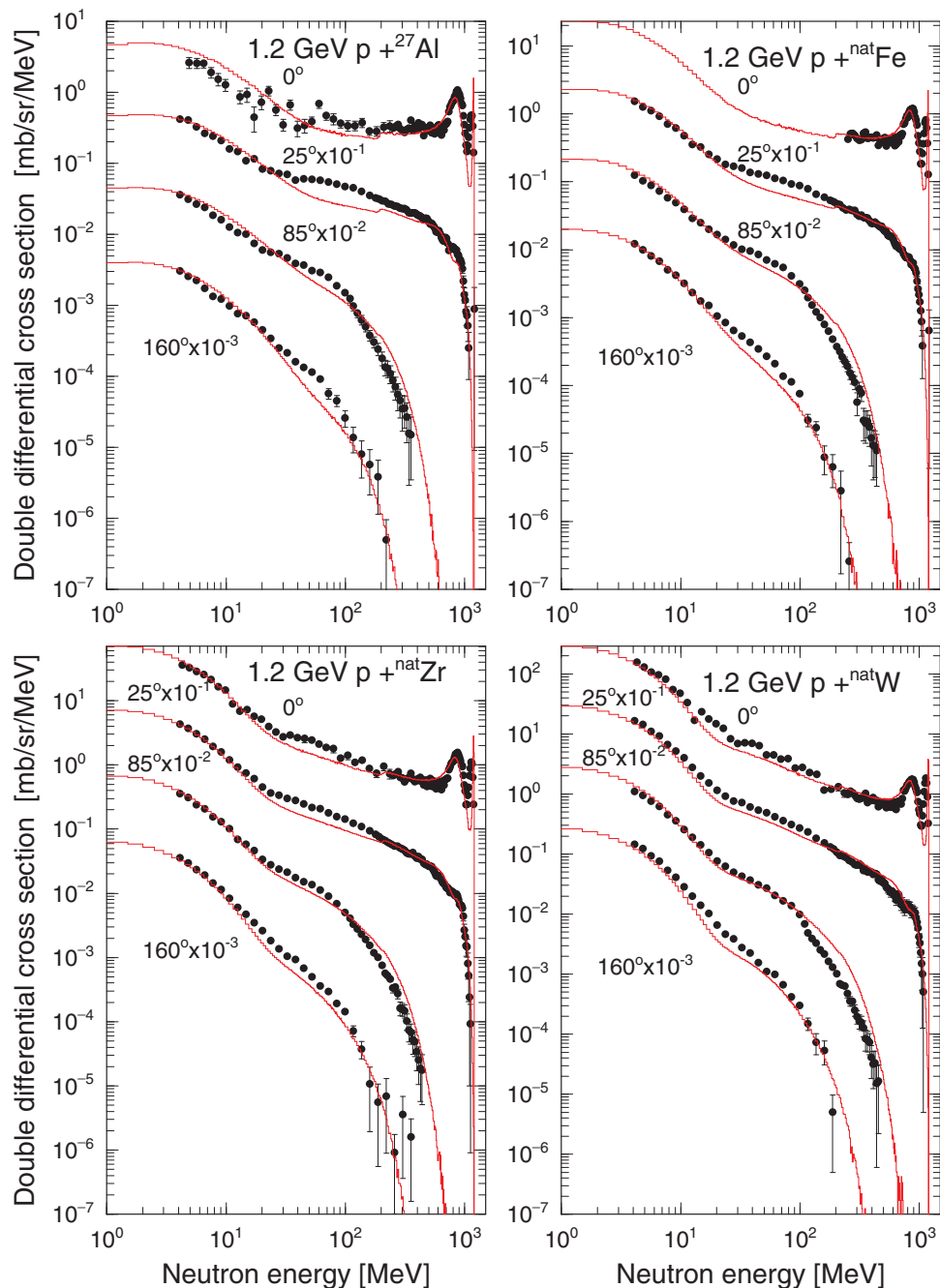


Figure 2. Double differential neutron production cross-sections of 1.2-GeV proton-induced reactions on Al, Fe, Zr, and W. The spectra have been multiplied by decreasing powers of 10, except for 0° . Experimental data was taken from a previous study [19].

Table 1. Experimental data-sets used for the benchmark calculations of the nuclear reaction model in PHITS. The DDXs denote the double differential cross-sections.

Projectile	Energy (MeV/u)	Targets	Observable	Figure
Proton	1200	^{27}Al , $^{\text{nat}}\text{Fe}$, $^{\text{nat}}\text{Zr}$, $^{\text{nat}}\text{W}$	DDXs-neutron	2
Proton	256	$^{\text{nat}}\text{C}$, ^{27}Al , $^{\text{nat}}\text{Fe}$, $^{\text{nat}}\text{Pb}$	DDXs-neutron	3
Proton	63	^{208}Pb	DDXs-neutron, proton, deuteron, triton, ^3He , ^4He	4
Proton	138	Li	DDXs-neutron	5
^{12}C , ^{16}O	290	$^{\text{nat}}\text{C}$	DDXs-neutron	6
Proton	1200	$^{\text{nat}}\text{Ni}$	DDXs-proton, deuteron, triton, ^3He , ^4He , Li	7
Proton	200	Ni, Au	DDXs-proton, ^4He	8
Proton	300, 500, 1000, 1500	$^{\text{nat}}\text{Fe}$	Mass distributions	9
Proton	1000	$^{\text{nat}}\text{Pb}$	Mass distributions	10

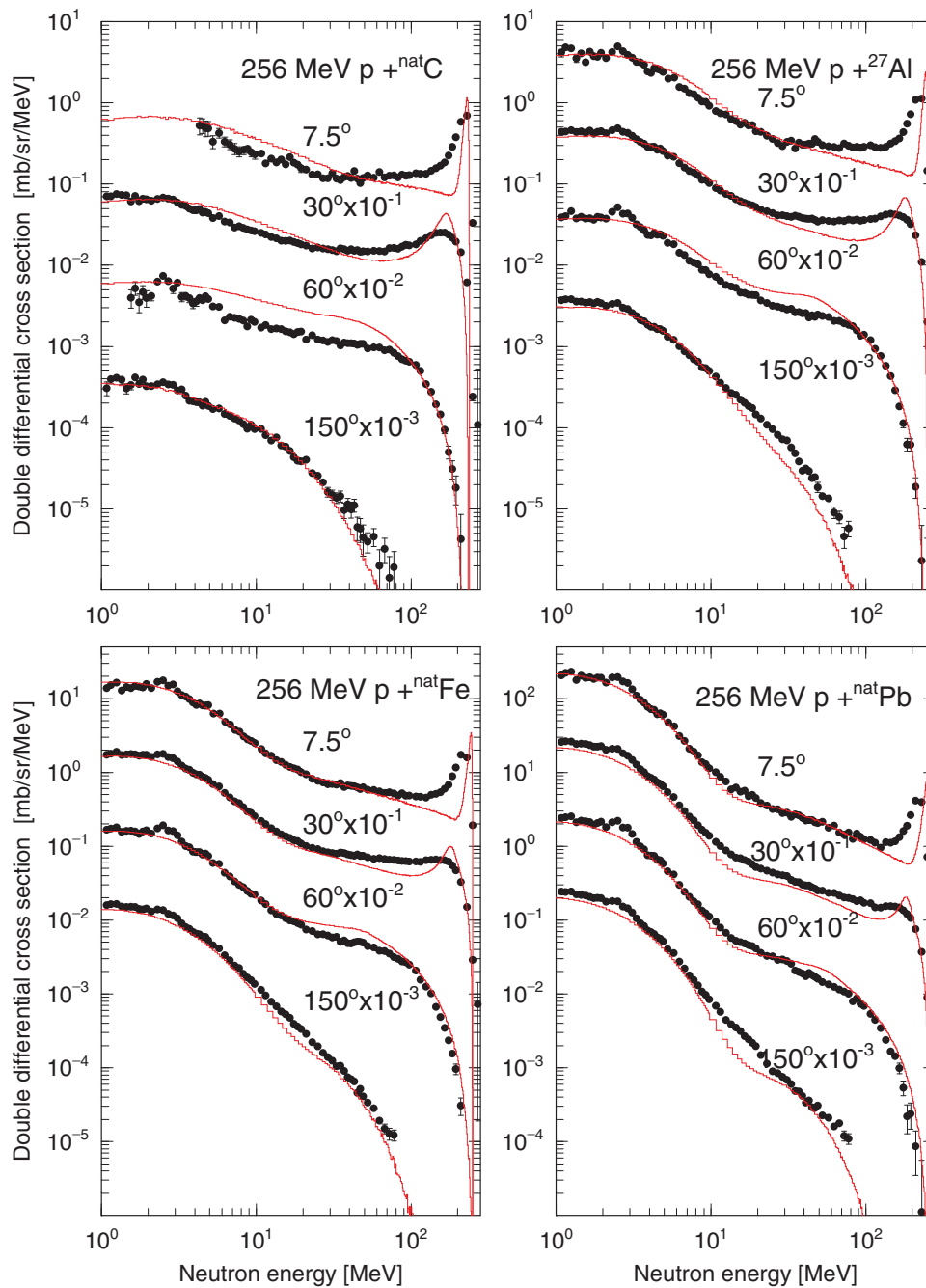


Figure 3. Double differential neutron production cross-sections of 256-MeV proton-induced reactions on C, Al, Fe, and Pb. The spectra have been multiplied by decreasing powers of 10, except for 7.5° . Experimental data was taken from a previous study [20].

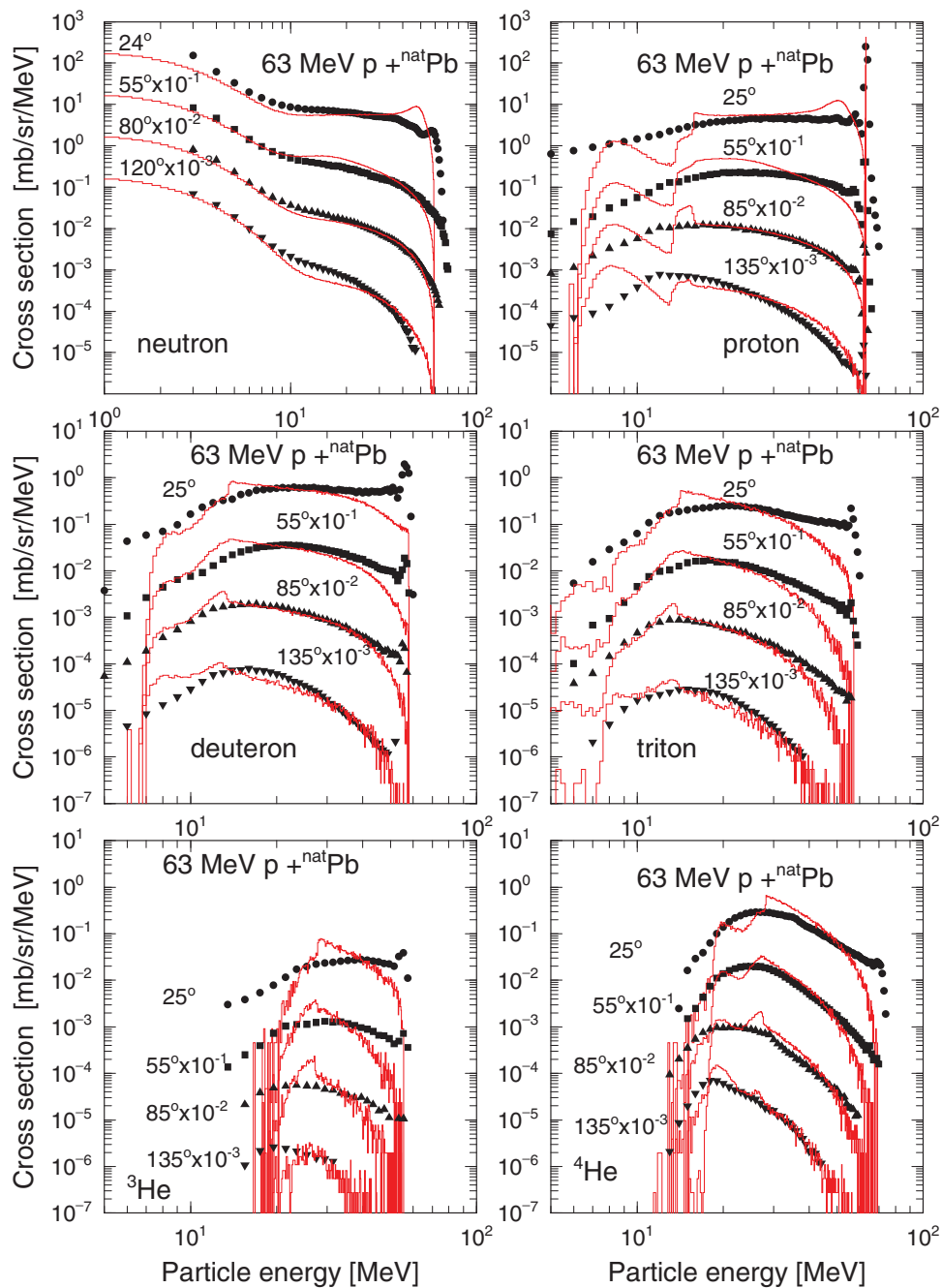


Figure 4. Double differential cross-sections of neutron, proton, deuteron, triton, ^3He , and ^4He for 63 MeV Pb(p,x) reactions. The spectra have been multiplied by decreasing powers of 10, except for 24° and 25° . Experimental data was taken from a previous study [22].

cascade (INC) models INCL4.6 [6] and JAM [12], which are described by approximately free-particle collisions within the nucleus, are used to simulate the dynamic stage of hadron- (nucleon and meson) induced nuclear reactions in the energy regions of 20 MeV–3 GeV

and 3 GeV–1 TeV, respectively. To describe the discrete levels of the excited nucleus for lighter targets such as Li, Be, and C, we have developed a computational model that combines the INCL model with a distorted-wave Born approximation (DWBA) [13,14].

Table 2. Experimental data-sets used to benchmark thick-target neutron yields and shielding.

Projectile	Energy (MeV/u)	Targets	Observable	Figure
Proton	256	$^{\text{nat}}\text{C}$, ^{27}Al , $^{\text{nat}}\text{Fe}$, ^{238}U , full stop length	Neutron energy spectra	11
Proton	40	$^{\text{nat}}\text{C}$, ^{27}Al , $^{\text{nat}}\text{Cu}$, $^{\text{nat}}\text{Pb}$, full stop length	Neutron energy spectra	12
p-Li neutron source	68	100, 150, 200 cm thick concrete 20, 40, 100 cm thick iron	Neutron energy spectra	13
p-Li neutron source	138	100, 150, 200 cm thick concrete 20, 40, 100 cm thick iron	Neutron energy spectra	13
Thick-target neutron produced by Hg(p,n) reaction	2830	Concrete, steel	Reduction rates	15

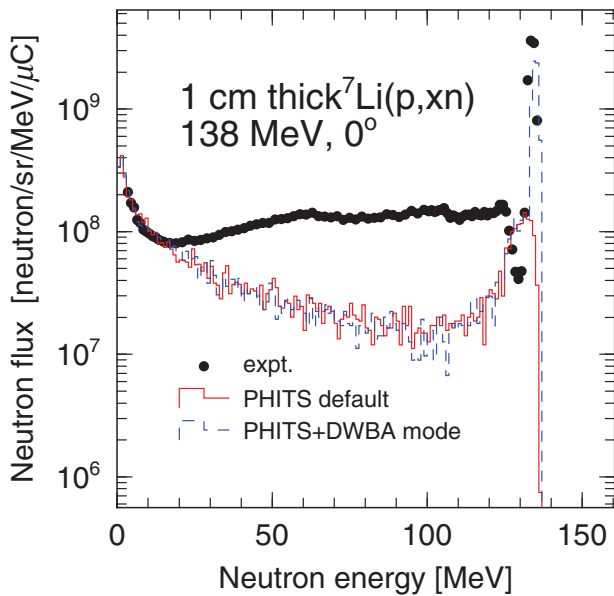


Figure 5. Comparison of neutron energy spectra calculated by INCL4.6 + GEM (solid line) and INCL4.6/DWBA + GEM (dashed line) with measurements for 138-MeV proton-induced reactions on a 1-cm-thick lithium target at 0° [24].

The quantum molecular dynamics model JQMD version 2 [10], which considers the time evolution of particles interacting each other, is generally employed for nucleus-induced reactions in the energy region of 10 MeV/u–1 TeV/u. The generalized evaporation and fission model (GEM) [15] is used for simulating the static stage of both the hadron- and nucleus-induced reactions. The energy losses of charged particles except for electrons and positrons are calculated using the

ATIMA [16] code with a continuous slowing down approximation.

Nuclear data libraries are generally used for simulating low-energy (10^{-5} eV–20 MeV) neutron-induced nuclear reactions. The data library is written in the ACE format, which is the same format as that adopted by the general-purpose Monte Carlo N-Particle code (MCNP) [17]. In the benchmark study, JENDL-4.0 in the ACE format was used for simulating low-energy neutron transportation in materials. Benchmark calculations for neutrons with energies below 20 MeV are beyond the scope of this study because they have already been extensively verified [11]. Photons, electrons, and positrons are transported using the EGS5 algorithm and database [7]. Photonuclear reactions [8] can be treated with energies from 2 MeV to 1 TeV. The lowest particle energy that can be simulated by PHITS is 1 keV because the continuous slowing down approximation cannot be applied to the transport simulation of charged particles below approximately this energy. It should be noted that this limitation does not apply to neutrons. Muon interaction models are recently implemented in PHITS, and the details of these models and the results of their benchmark calculations have previously been shown [18].

In this paper, the satisfactory agreement between the simulations and the measurements is defined as a factor of 2–3 for nuclear reaction models such as INCL and several % for atomic interaction models such as the EGS5 algorithm. The statistical uncertainty of the calculations is sufficiently small (a few %) for the data used in the discussion of discrepancy between the experimental data and the calculated results in this

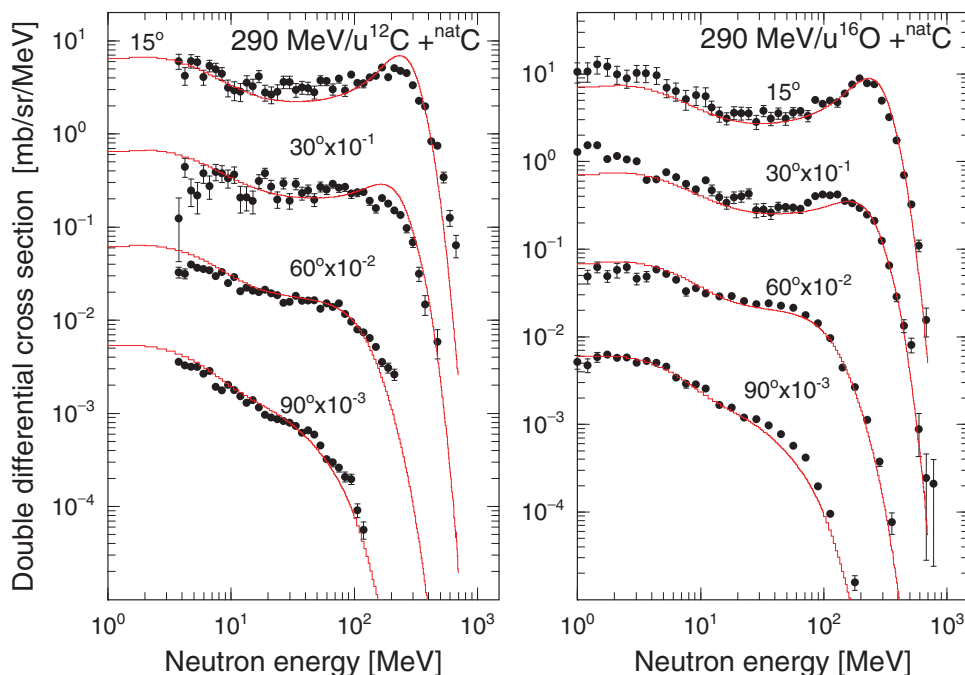


Figure 6. Double differential neutron production cross-sections of 290-MeV/u ^{12}C - and ^{16}O -induced reactions on a carbon target. The spectra have been multiplied by decreasing powers of 10, except for 15° . Experimental data was taken from a previous study [26].

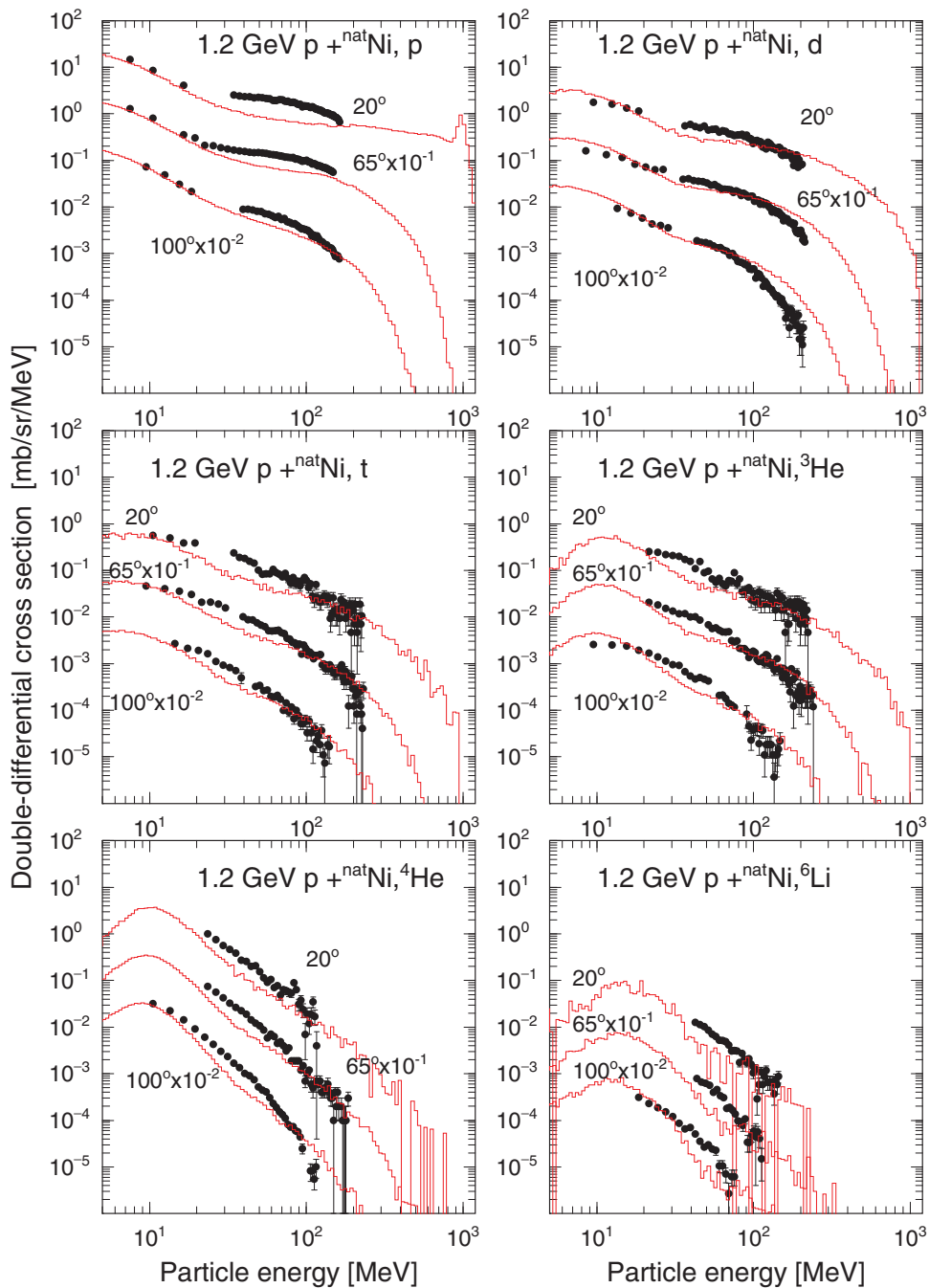


Figure 7. Double differential cross-sections of proton, deuteron, triton, ${}^3\text{He}$, ${}^4\text{He}$, and ${}^6\text{Li}$ for a 1.2-GeV Ni(p,x) reaction and detection angles from 20° to 100° . The spectra have been multiplied by decreasing powers of 10, except for 20° . Experimental data were taken from a previous study [27].

study. Further, there is a large statistical uncertainty for particle with high energies in the particle energy spectrum; however, this is not important for the current discussion.

3. Benchmark for particle production cross-sections

In this section, we focus on the benchmark calculations of particle production cross-sections. Table 1 lists the experimental data-set (9 cases) used as the benchmark for the nuclear reaction model. The calculations in this section were performed by coupling

INCL4.6 with GEM for proton incident reactions and the JQMD model with GEM for heavy-ion incident reactions.

3.1. Neutron production cross-sections

Figures 2 and 3 show results calculated for the double differential neutron production cross-sections of 1.2 GeV and 256 MeV proton-induced reactions [19,20] on a few targets.

The spectrum at the forward angles is characterized by peaks at the highest neutron energy in the forward

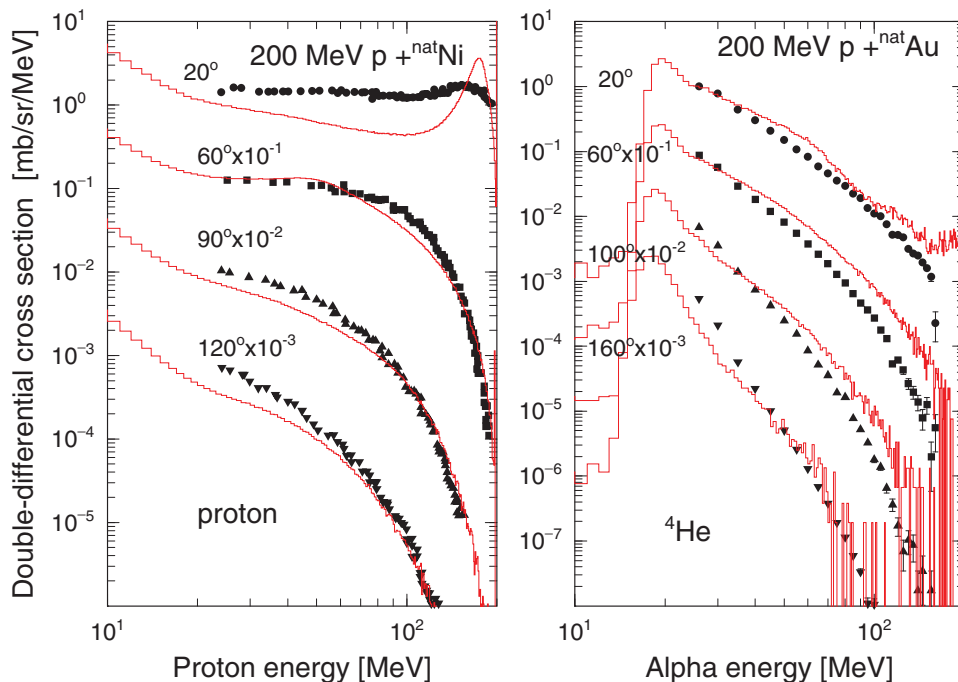


Figure 8. Double differential cross-sections of 200-MeV Ni(p,p) [28] and Au($p,^4\text{He}$) [29] reactions. The spectra have been multiplied by decreasing powers of 10, except for 20° .

direction [21]. The quasi-elastic peak is located at energies close to that of the incident projectile. This is the result of a direct interaction between the projectile and a neutron in the nucleus. The broad peak located slightly below the quasi-elastic peak for a 1.2-GeV proton is associated with pion emission through

an excitation of the Δ (1232 MeV) resonance in inelastic nucleon–nucleon collisions [21]. PHITS can reproduce the experimental data well except for the neutron spectra in the energy region from approximately 30 to 200 MeV. According to a study of a surface coalescence model incorporated in the INCL4.6 model

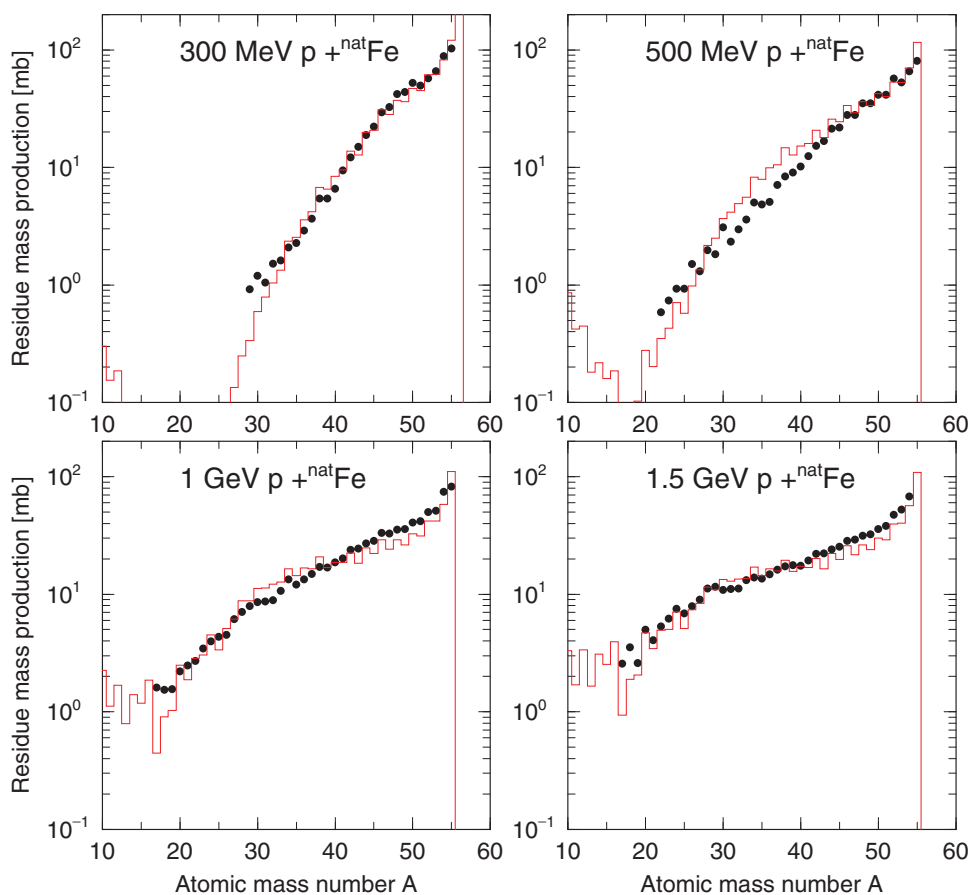
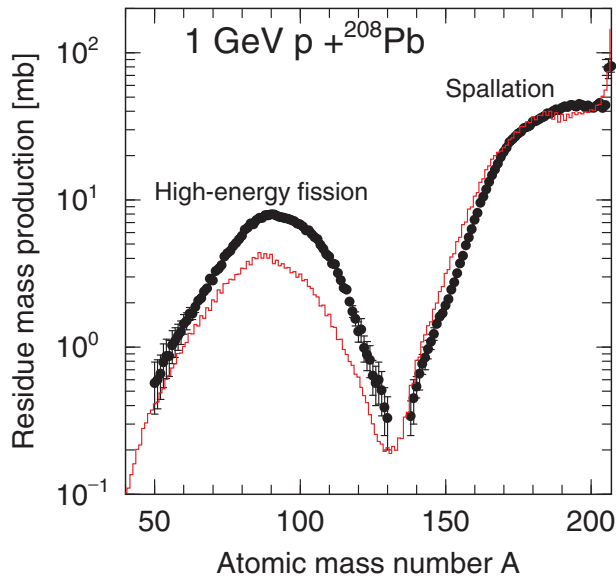


Figure 9. Mass distribution of nuclides for the 300 MeV, 500 MeV, 1 GeV, and 1.5 GeV Fe(p,x) reactions [30].

Table 3. Experimental data-sets used to benchmark an electromagnetic cascade.

Projectile	Energy (MeV)	Targets	Observable	Figure
Electron	1	Be, Al, Fe, Au	Photon energy spectra	17
Electron	15	Be, Al, Pb	Photon energy spectra	18
Photon	60, 300	Ca, Cu	Proton energy spectra	19
Electron	150	Pb	Neutron energy spectra	20
Electron	2040	C, Al, Cu, Pb	Neutron energy spectra	21
Electron	0.015–0.050	Si	Depth–dose	22
Electron	10,20	Water, air, Al	Depth–dose	23

**Figure 10.** Mass distribution of nuclides for the 1-GeV $Pb(p,x)$ reaction [31].

[6], clusters in the cascade stage are formed at the expense of the production of neutrons and protons. An underestimation therefore appears in this energy region.

The upper left part of Figure 4 shows the double differential neutron production cross-sections of the 63-MeV $Pb(p,n)$ reaction. The results from PHITS are generally in acceptable agreement with the experimental data [22], except for a peak spectrum at 24° . This is because INCL4.6 cannot appropriately reproduce the quasi-elastic scattering [23]. The benchmark calculations for charged particle production shown in the other parts of Figure 4 are discussed in the next subsection.

Figure 5 shows a comparison of the neutron energy spectra calculated for 138-MeV proton-induced reactions on a 1-cm-thick lithium target at 0° with the experimental data [24]. Quasi-monoenergetic neutron sources using a ${}^7Li(p,n){}^7Be$ reaction are employed for calibrating the neutron detectors, shielding benchmark experiments, and the soft error analysis on the semiconductor. It should be noted that INCL4.6 (solid line) cannot predict the monoenergetic neutron spectrum produced by the discrete levels of the excited nucleus for the ${}^7Li(p,n){}^7Be$ reaction. Consequently, the

DWBA mode can reproduce the peak neutron energy spectrum at forward angles (dashed line in Figure 5), which is the summation of neutrons produced by the discrete levels of 7Be . However, it cannot reproduce the neutron energy spectra for continuous part for energies from 20 MeV to below the peak. To predict the neutron energy spectra over a wide-energy range of proton incident reactions on lighter targets, we plan to incorporate the high-energy version of the evaluated proton and neutron data library JENDL-4.0/HE, which has energies up to 200 MeV [25], in the PHITS package.

Figure 6 shows predictions of the double differential neutron production cross-sections of the 290-MeV/u ${}^{12}C$ - and ${}^{16}O$ -induced reactions on a carbon target compared to measurements taken from a previous study [26]. The JQMD + GEM model reproduces the experimental data well over the wide-energy and angle regions.

3.2. Charged particle production cross-sections

Benchmarks were considered for light charged particle productions such as proton, deuteron, triton, 3He , 4He , and 6Li . Figure 7 shows a comparison of the PHITS prediction and the experimental data for the double differential cross-sections of light charged particles for the 1.2-GeV $Ni(p,x)$ reaction [27]. Figure 8 shows the double differential cross-sections of the 200-MeV $Ni(p,p)$ [28] and $Au(p,{}^4He)$ reactions [29], respectively. To describe the emission of charged clusters during the dynamic stage in the nucleon–nucleus reactions, a surface coalescence model was developed and incorporated into INCL4.6, which was verified to reproduce the experimental data for lighter charged particles [6]. Therefore, the results from PHITS were in good agreement with the cross-sections of the charged particles.

As shown in the lower panels of Figure 4 [22], PHITS cannot reproduce the experimental data for light charged particles for a 63-MeV $Pb(p,x)$ reaction, particularly at the energy range between 10 and 30 MeV. This is because the Coulomb barrier height in INCL4.6 was not adjusted so as to reproduce a charge particle spectrum for low-energy (below 100 MeV) proton incident reactions on heavy targets [6].

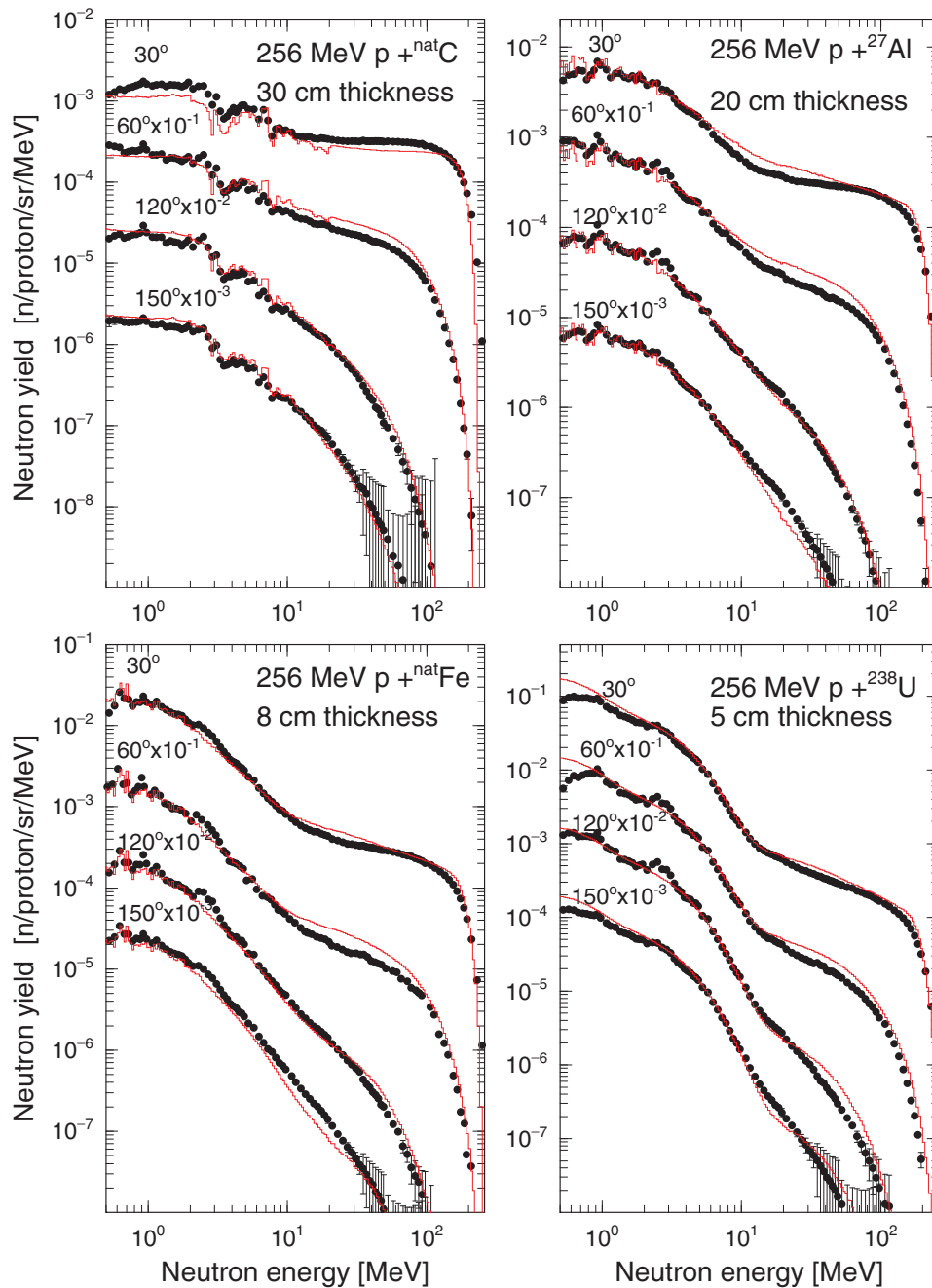


Figure 11. Differential neutron production yields at scattering angles of 30° , 60° , 120° , and 150° for an incident proton energy of 256 MeV on stopping lengths of C, Al, Fe, and U targets [33].

3.3. Mass distribution of nuclides produced by nuclear reactions

Figures 9 and 10 show the mass distribution of nuclides for 300 MeV, 500 MeV, 1 GeV, and 1.5 GeV $Fe(p,x)$ [30] and 1 GeV $Pb(p,x)$ [31], respectively. The measurements were performed at Gesellschaft für Schwerionenforschung mbH (GSI) using an inverse kinematics method [30,31]. Results calculated by INCL4.6 for the mass distribution of spallation products agree well with the experimental data. However, PHITS does not reproduce the width and heights of the

distributions of the high-energy fission products peaking at a range around an atomic mass $A = 90$. This is because the initial version of GEM [12], which is implemented in PHITS, does not correctly describe nuclide production in the fission region. To account for high-energy fission, the fission model in GEM2 was improved [32] so as to reproduce the mass distributions of fission fragments with 50% accuracy. We will implement the improved GEM model into PHITS to describe the high-energy fission process more precisely.

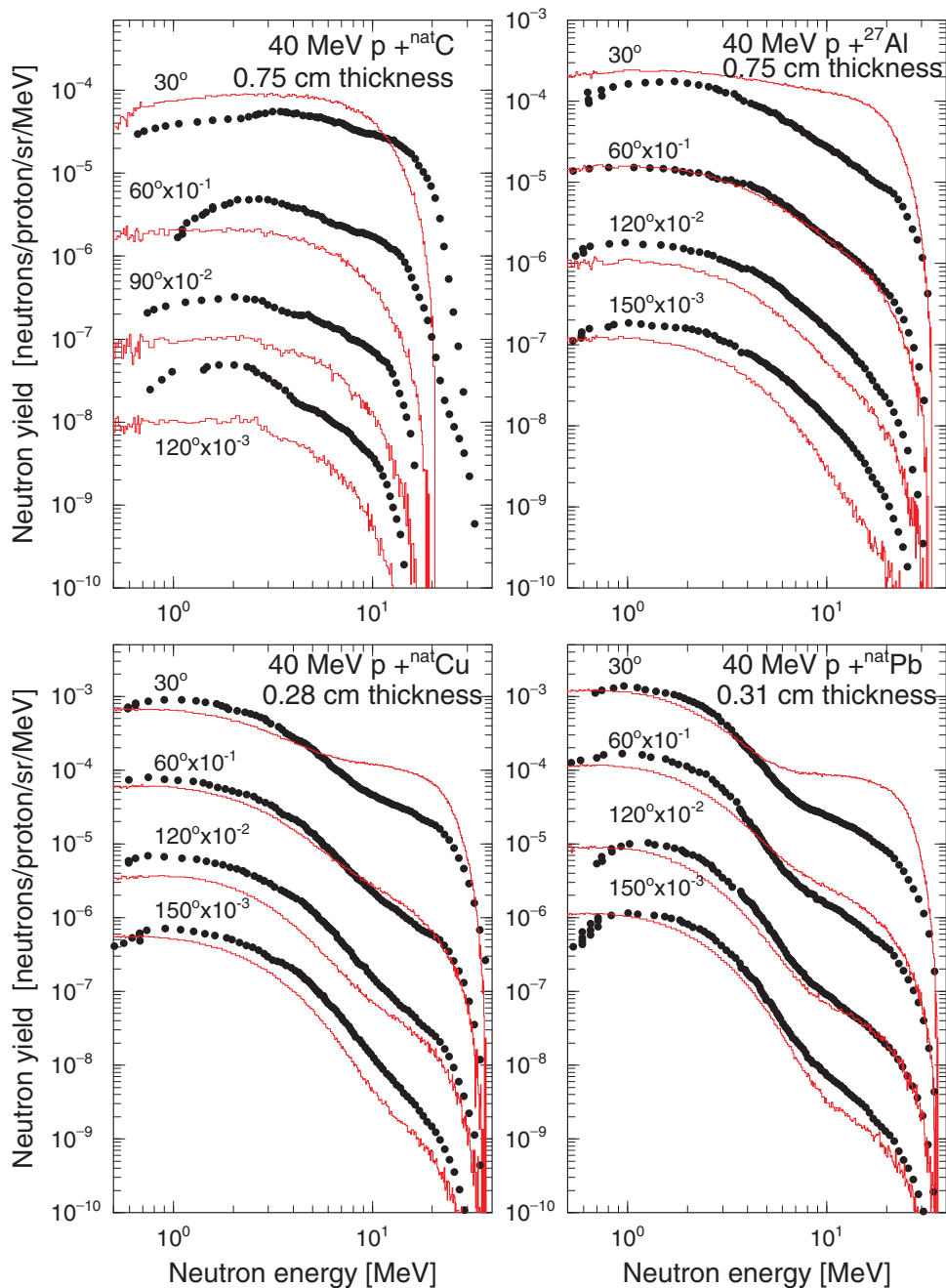


Figure 12. Differential neutron production yields at scattering angles of 30° , 60° , 120° , and 150° for an incident proton energy of 40 MeV on stopping lengths of C, Al, Cu, and Pb targets [34]. The solid line shows results calculated by INCL4.6 + GEM.

4. Benchmark for neutron shielding experiments

Although the cross-sections calculated with the thin targets discussed in Section 3 are useful in validating the nuclear reaction models in PHITS, the experimental data produced by thick targets, extended so as to be sufficiently large to generate a particle cascade inside the target, are mainly performed for validating particle transportation in materials in the wide-energy region. Table 2 lists the experimental data-set (5 cases) used to benchmark thick-target neutron yields and shielding experiments.

4.1. Thick-target neutron yields

Figure 11 shows the differential neutron production yields at scattering angles of 30° , 60° , 120° , and 150° for an incident proton energy of 256 MeV on the stopping lengths of the C, Al, Fe, and U targets [33]. In general, the agreement between the PHITS results and that of the experimental data is fairly good, except for the energy range below 1 MeV for uranium, where the calculated results are approximately 50% higher than those of the experimental data. In contrast, for the cases pertaining to 40-MeV proton incidence on the stopping lengths of the C, Al, Cu, and Pb targets [34], as

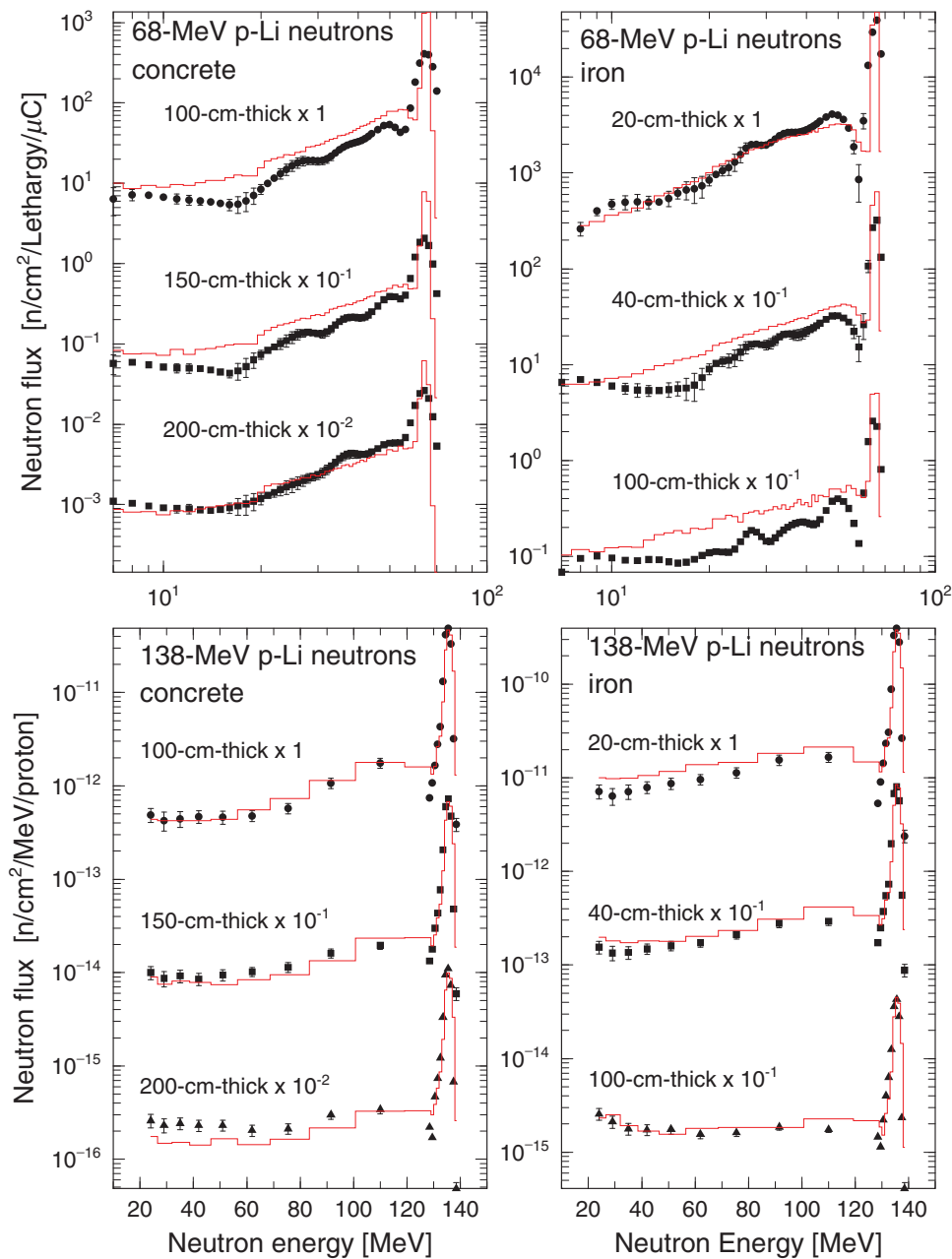


Figure 13. Neutron energy spectra transmitted through concrete and iron shields of various thicknesses on the beam axis between experiments and PHITS calculations for 68- [36,37] and 138-MeV [38] p-Li neutron sources.

shown in Figure 12, the agreement between the PHITS results and the experimental data is not good, particularly at the forward angle. For an incident proton energy below approximately 100 MeV, it is better to use the evaluated proton and neutron data libraries, such as JENDL-HE/2007 [35] rather than INCL4.6 because the treatment of the first collisions in INCL4.6 is not suitable for the low-energy region below approximately 100 MeV, as is shown in Figure 12.

4.2. Shielding experiments

Neutron energy spectra that penetrated through concrete and iron-shield assemblies were measured at

the cyclotron facility of the Takasaki Ion Accelerator for Advanced Radiation Research (TIARA) using a 68-MeV ${}^7\text{Li}(p,n){}^7\text{Be}$ monoenergetic neutron source (p-Li neutron source) [36,37], and it was measured at the cyclotron facility of Research Center for Nuclear Physics (RCNP), Osaka University, using an 138-MeV p-Li neutron source [38,39].

At TIARA, concrete and iron shields (width: 120 cm and height: 120 cm) were settled at the collimator exit, changing the thickness from 25 to 200 cm for concrete [36] and from 10 to 130 cm for iron [37]. At RCNP, iron and low-activation concretes were assembled with thicknesses of 10–100 cm for the iron shield and from 25 to 200 cm for the low-activation concrete shield. The densities of the iron and low-activation concrete

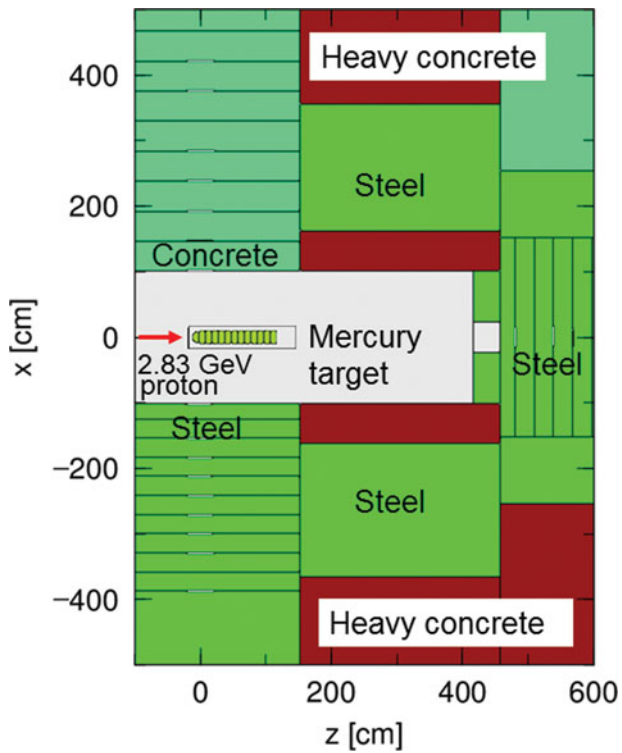


Figure 14. PHITS geometry for a horizontal cut through the shielding arrangement of steel and concrete shields around the thick mercury target (diameter = 20 cm and length = 130 cm) of the AGS-Spallation Target Experiment (ASTE) collaboration at the AGS accelerator at BNL [40].

were 7.87 and 2.33 g/cm³, respectively, and the atomic compositions of these shields are listed in a previous study [38,39].

In the PHITS calculations for these experiments, the experimental p-Li neutron source was employed as a source term [36] because INCL4.6 cannot reproduce the neutron energy spectrum produced by discrete levels of excited nuclei, as shown in Figure 5. Figure 13 shows a neutron energy spectra transmitted through concrete and iron of various thicknesses on the beam axis between the experimental data and the PHITS results for a 68- [36,37] and 138-MeV [38] p-Li neutron source. Agreements are generally within a factor of two; however, some discrepancies were observed for the 68-MeV case. For neutron spectra that penetrated through the 100- and 150-cm-thick concrete shields with the 68-MeV p-Li neutron source, the PHITS results overestimated the experimental data, particularly in the peak region. For the iron shields, agreement worsens as the thickness of the shield increases. Therefore, it is better to employ the high-energy evaluated nuclear data libraries, such as JENDL-HE/2007 [35] instead of using the INCL4.6 model with energies below approximately 100 MeV.

The AGS-Spallation Target Experiment (ASTE) collaboration [40] conducted a shielding experiment [41] using a 2.83-GeV proton beam incident onto an ASTE

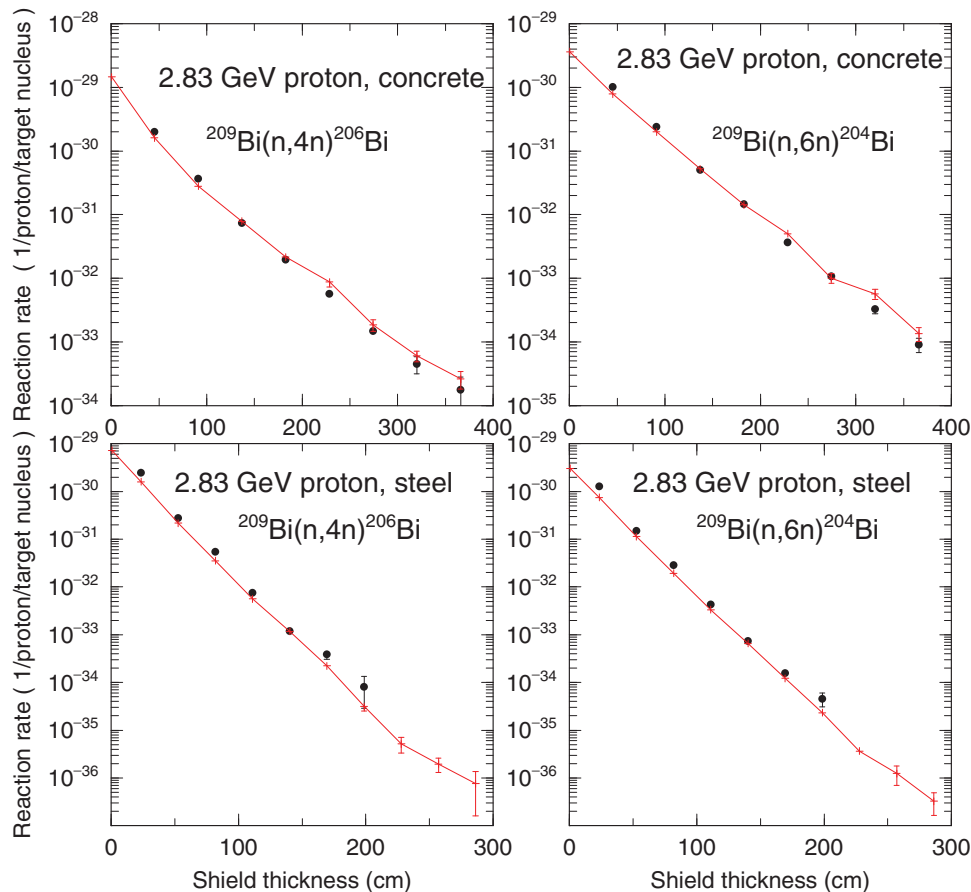


Figure 15. Depth-dependent $^{209}\text{Bi}(n,4n)$ and $^{209}\text{Bi}(n,6n)$ reaction rate distributions in concrete and steel shields in Figure 14 [41].

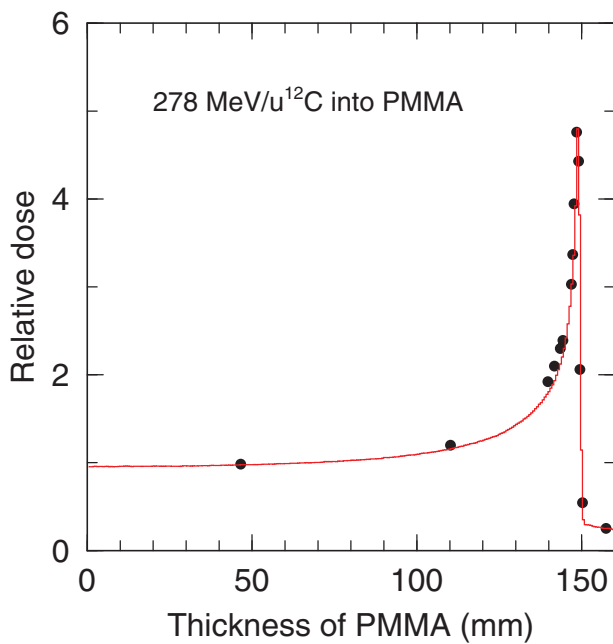


Figure 16. Depth-dose distribution of 278-MeV/u ^{12}C beams into polymethyl methacrylate. The lines and circles denote the dose calculated by PHITS and that measured by the ionization chamber, respectively [42].

bare mercury target, with steel and ordinary concrete shields placed at lateral positions to the target. Figure 14 shows the calculation arrangement of the steel and ordinary concrete shielding surrounding the mercury target. The lateral shields of ordinary concrete (thickness: 5.0 m) and steel (thickness: 3.3 m) were placed at a distance of 1 m from the mercury target. All shields had cross-sections more than $2 \times 2 \text{ m}^2$, with densities of steel and concrete of 7.74 and 2.45 g/cm^3 , respectively. In the experiments, the spatial neutron flux attenuation inside the shielding was determined by the reaction rate distributions of the activation samples of the $^{27}\text{Al}(n,\alpha)^{24}\text{Na}$, $^{115}\text{In}(n,n')^{115\text{m}}\text{In}$, $^{197}\text{Au}(n,\gamma)^{198}\text{Au}$, and $^{209}\text{Bi}(n,xn)$ reactions. In these calculations, the reaction rates were derived by multiplying the activation reaction cross-sections [4] with the calculated neutron spectra. Figure 15 shows the distributions of depth-dependent $^{209}\text{Bi}(n,4n)$ and $^{209}\text{Bi}(n,6n)$ reaction rates in the concrete and steel shields in Figure 14 [41]. The $^{209}\text{Bi}(n,4n)$ and $^{209}\text{Bi}(n,6n)$ reactions cover the neutron energy range over 24 and 42 MeV, respectively. The PHITS results of the depth-dependent $^{209}\text{Bi}(n,4n)$ and $^{209}\text{Bi}(n,6n)$ reaction rate distributions in the concrete and steel shields are in close agreement with the experimental data.

5. Benchmark for depth-dose distribution for radiotherapy using ^{12}C beam

The validation of dose as a function of the body depth is required for a precise estimation of the clinical effect on radiotherapy using heavy-ion beams. Figure 16 shows

the depth-dose distributions of the PHITS calculations as compared to the experimental data at the National Institute of Radiological Sciences for 278 MeV/u (nominal energy of 290 MeV/u) ^{12}C incident on polymethyl methacrylate (PMMA) performed with an ionization chamber [42].

In the PHITS's calculation, the energy loss of the charged particles in the materials was calculated using the ATIMA code with a continuous slowing down approximation [13]. The energy straggling [43,44] and the Coulomb multiple scattering [45] were considered in ATIMA. In this case, the depth-dose calculated by PHITS agreed well with the experimental data. More benchmark results on ATIMA are given in [46].

6. Benchmark for electron and photon transportation

Table 3 lists the experimental data-set (7 cases) used to benchmark the electromagnetic cascade and photonuclear reaction. The experimental cases presented in this section are grouped into three categories: (1) thick-target bremsstrahlung spectra (Figures 17 and 18), (2) proton and neutron energy spectra produced by photonuclear reactions (Figures 19–21), and (3) transmission and absorption of electrons (Figures 22 and 23). The experiments in group (1) mostly serve to validate the model and sampling algorithm for the bremsstrahlung emission and the transport of the generated photons within the sample. The benchmarks in group (2) aim to validate the photonuclear reactions and the transportation of the generated neutrons in the material slab. The benchmarks in group (3) aim to probe the balance between the energy loss and the angular deflection required to describe the energy angular distributions of the electrons in the irradiated material slabs. All benchmark calculations were performed using the EGS5 mode [7] in PHITS.

6.1. Electron bremsstrahlung

In this subsection, we report on the photon and electron spectra via electron bremsstrahlung. Figure 17 shows a comparison of the thick-target bremsstrahlung spectra for 1-MeV electron incidence on the 0.3-cm-thick beryllium, 0.2-cm-thick aluminum, 0.078-cm-thick iron, and 0.039-cm-thick gold targets [47]. The calculated results agree well with the experimental data over a wide range in each angle. For the gold target, in the photon energy region below approximately 0.25 MeV, the spectra proceed to a lower intensity at angles from 30° to 60° due to the greater attenuation in the increasing thickness of the target material as the photon angle is increased [47]. This tendency is not well reproduced by PHITS (Figure 17).

Figure 18 shows the thick-target bremsstrahlung spectra for a 15-MeV electron incidence on the

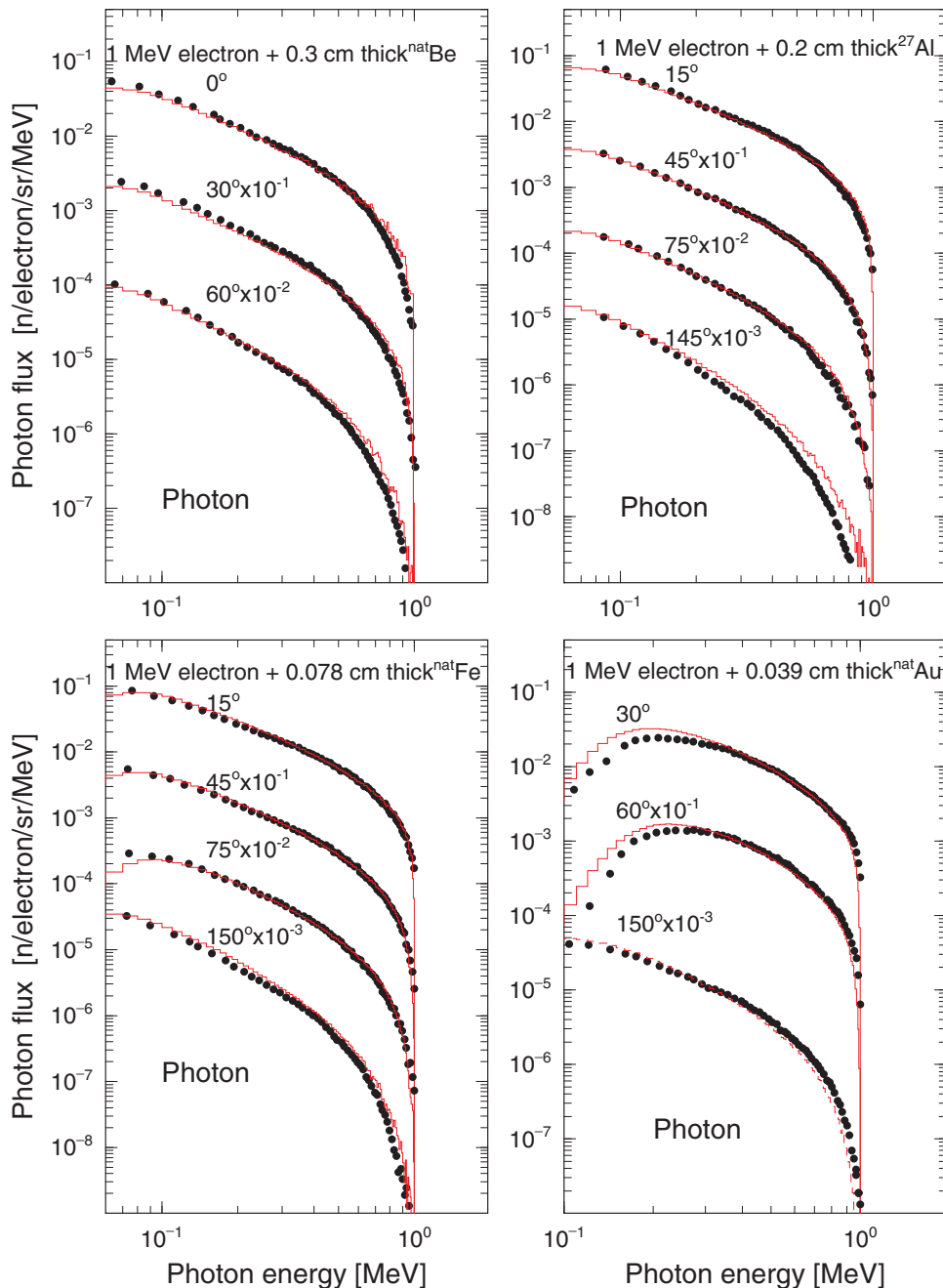


Figure 17. Bremsstrahlung energy spectra for a 1-MeV electron beam incident on Be, Al, Fe, and Au foils of the indicated thicknesses. Circles are experimental results from a previous study [47].

3.6-cm-thick aluminum and 0.8-cm-thick lead targets [48]. The 0.511-MeV photons generated by the annihilation of electrons and positrons in the targets appeared in the PHITS calculations and the experimental data. A peak at 0.511 MeV does not appear well in the experimental data due to the poor energy resolution of the experiment. For an aluminum target, there was good agreement between the experimental values and the calculations observed over a wide range of angles. For a lead target, the calculated results underestimated the experimental data with decreasing photon energies in the energy region below 0.3 MeV. According to Faddegon et al. [48], the excessive number of photons in this energy region can be attributed to the collimator effects

scattering from objects near the target, which are not considered in the PHITS simulation.

6.2. Photonuclear reaction

In this subsection, we report on the proton and neutron spectra obtained via photonuclear reactions. Figure 19 shows double differential cross-sections of protons for a 59.3–65.2-MeV photon incident reaction on calcium [49] and a 300-MeV photon incident reaction on copper [50]. The photonuclear reaction in PHITS [8] reproduces the proton yields well for these cases, except for the case of 45°. Figures 20 and 21 show neutron yields for 150-MeV [51] and 2.04-GeV [52]

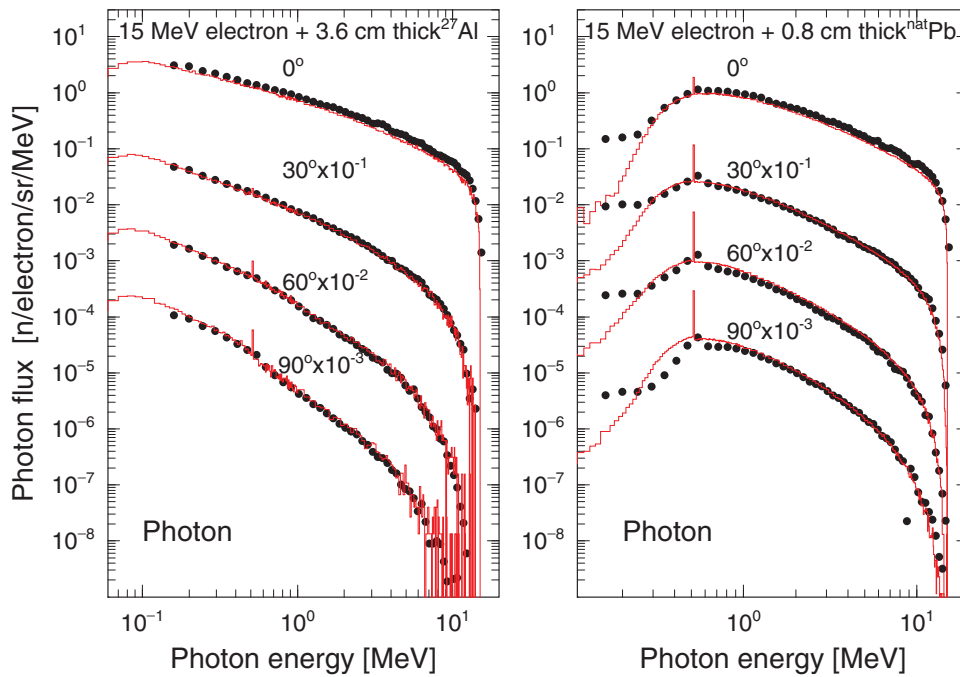


Figure 18. Photon yields for the reaction of 15-MeV electron on 3.6-cm-thick aluminum and 15-MeV electron on 0.8-cm-thick lead [48].

electron incidence on thick targets. Secondary photons in materials are generated by electron bremsstrahlung. Subsequently, the neutrons are generated by a photonuclear reaction. In all cases, PHITS's results underestimated the experimental data. It should be noted that the photonuclear reaction cross-section is much less than the photoatomic reaction cross-section, and hence it is difficult to obtain sufficient statistics in these calculations. Therefore, the photonuclear reaction cross-section

is biased by setting a parameter-pnimul, which is the multiplying factor to increase sampling probability of a photonuclear reaction in these calculations.

6.3. Transmission and absorption of electrons

This subsection reports on the benchmark examples for the depth-dose in materials. Figure 22 shows the depth-dose distributions at the central axis of Si for

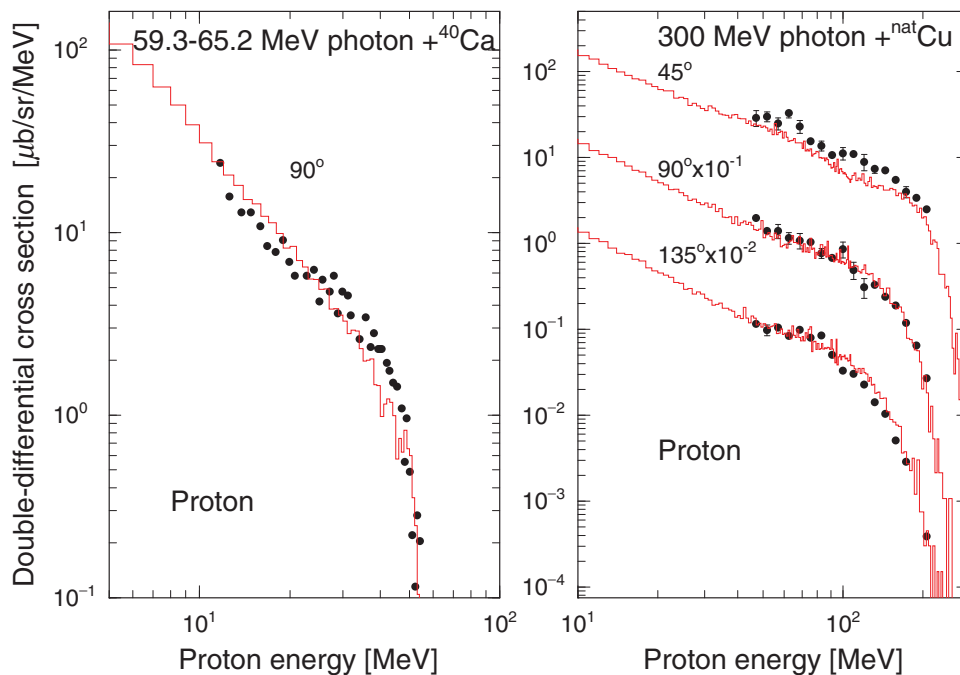


Figure 19. Double differential cross-sections of protons for a 59.3–65.2-MeV photon incident reaction on Ca [49] and a 300-MeV photon incident reaction on Cu [50].

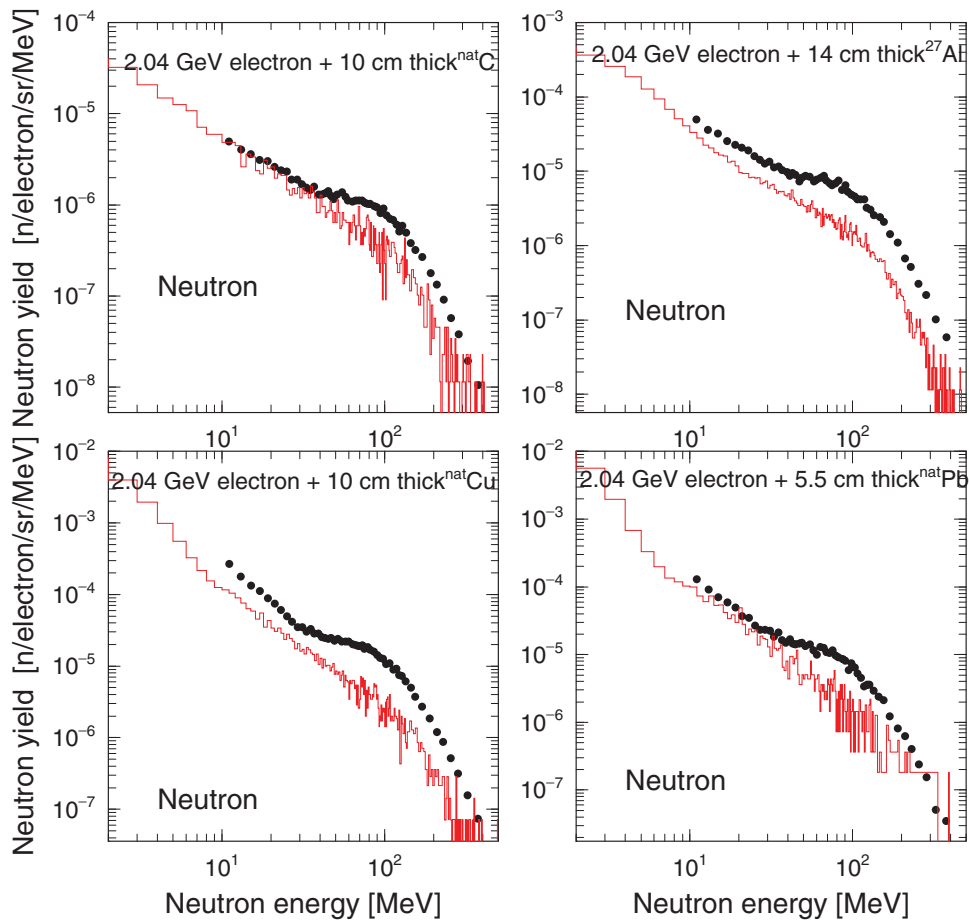


Figure 21. Neutron yields for the reaction of 2.04-GeV electron and thick C, Al, Cu, and Pb [52].

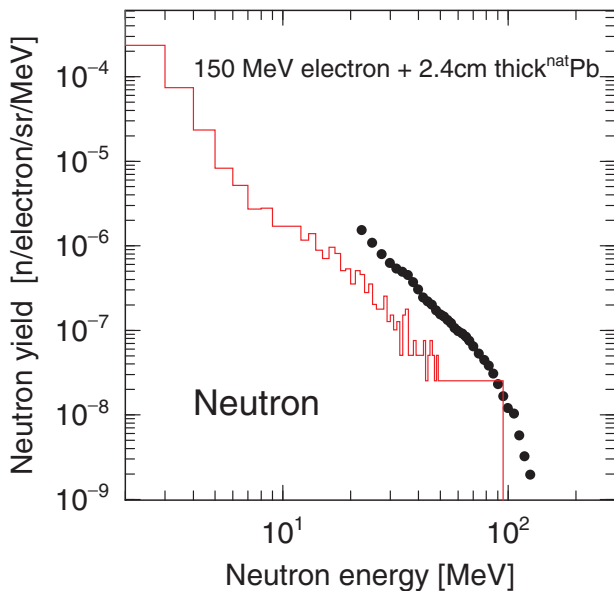


Figure 20. Neutron yields at 90° for the reaction of 150-MeV electron and 2.4-cm-thick Pb [51].

an electron beam with energies of 15, 30, 40, and 50 keV [53,54]. The cut-off energy of the electrons and positrons was set to 1 keV. The agreement between the simulations and experiments is satisfactory.

Figure 23 shows the depth-dose distributions at the central axis of a water cylinder uniformly irradiated by

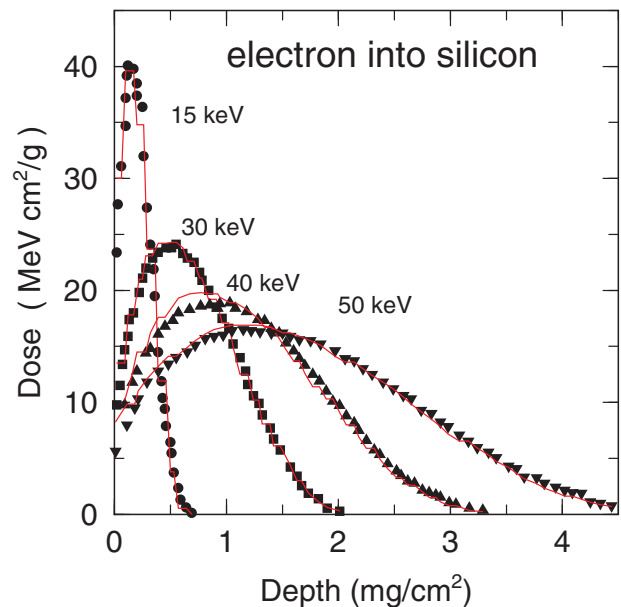


Figure 22. Depth-dose distributions at the central axis of Si for an electron beam with energies of 15, 30, 40, and 50 keV [53,54].

a 10 and 20 MeV electron beam [55,56]. The cut-off energy of the electrons and positrons was set to 50 keV. A water cylinder comprises a cylindrical disc (air with diameter = 1 cm and length = 2 cm or aluminum with diameter = 1 cm and length = 1 cm) inserted at

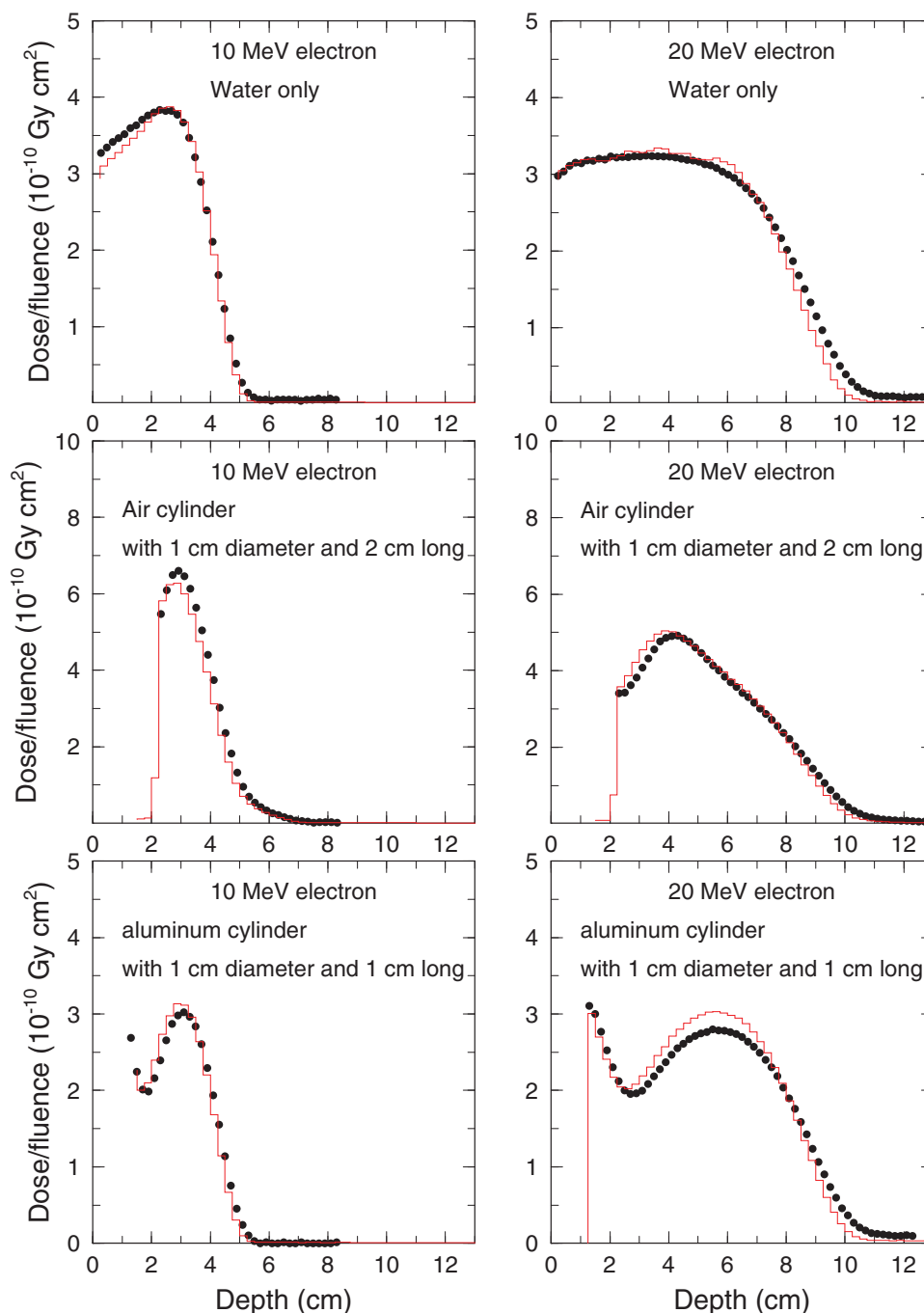


Figure 23. Depth–dose curves for 10 and 20 MeV electron incidences into pure water, water containing air, or an Al cylindrical disc inserted 2 mm behind the front surface [55,56].

a distance 2 mm behind the front surface. The agreement between the experimental data and the calculated results in Figure 23 is also satisfactory, and the results calculated with PHITS are nearly identical to those calculated with the original EGS5 code discussed in an earlier study [56].

7. Summary

We performed benchmark calculations for 58 cases related to various different fields, such as accelerator design and medical physics, using the models recommended for use in the recent version of PHITS (version 2.88). Twenty-two cases are reported in

figures of this paper and 36 cases are reported in online as supplementary materials of this paper. The combination of the intranuclear cascade model INCL4.6 with the evaporation model GEM can generally reproduce neutron and charged particle yields produced by proton and heavy-ion beams with energies above 100 MeV/u, except for the p-Li reaction. For the shielding benchmark experiments with p-Li neutron sources at TIARA and RCNP, the calculated neutron energy spectra generally agreed well with the experimental data at a variety of depths in a shield within a factor of two.

For the mass distributions of the nuclides by the high-energy (above 100 MeV) proton incident reactions on Fe and Pb targets, the calculated mass

distributions of the spallation products agree well with the experimental data. Conversely, for a 1-GeV proton incident reaction on Pb, PHITS does not reproduce the distributions of the high-energy fission products because GEM in PHITS does not appropriately describe nuclide production in the fission process. For the depth-dose distribution in water using a 278 MeV/u ^{12}C beam, results calculated with the energy loss model ATIMA agreed well with the experimental data. For electromagnetic cascades with energy ranging from keV to GeV, PHITS employed the EGS5 mode in order to reproduce the experimental data well, except for the case where neutrons were produced by photonuclear reactions.

The results of the benchmark study suggested several tasks for further developing PHITS. The evaluated nuclear data library JENDL-4.0/HE [25] for proton and neutron energies up to 200 MeV should be incorporated into the PHITS package in order to improve the accuracy of particle production particularly with energies below 100 MeV, and interactions of particle with lighter targets such as Li and Be targets. To better calculate neutron production from photonuclear reactions, the JENDL Photonuclear Data file (JENDL/PD) [57] is also desirable to be incorporated in the PHITS package. Improvement of the GEM model is also regarded so that it describes nuclide production in the fission.

All benchmarking results in this study are provided as supplementary materials online.


Acknowledgments

We wish to thank Dr H. Iwase, Prof. Y. Namito, and Prof. H. Hirayama of KEK for their advices on the benchmark of electron and photon transports. We also wish to thank Dr M. Hagiwara of KEK, Dr S. Kunieda of JAEA, and Dr F. Nobuhara of Tokyo Nuclear Services Co., Ltd. for providing information on the input file for the shielding experiment.

Disclosure statement

No potential conflict of interest was reported by the authors.

ORCID

Yosuke Iwamoto  <http://orcid.org/0000-0003-4688-6508>

References

- [1] Sato T, Niita K, Matsuda N et al. Particle and heavy ion transport code system, PHITS, version 2.52. *J Nucl Sci Technol.* 2013;50:913–923.
- [2] Iwase H, Niita K, Nakamura T. Development of general-purpose particle and heavy ion transport Monte Carlo code. *J Nucl Sci Technol.* 2002;11:1142–1151.
- [3] Niita K, Matsuda N, Iwamoto Y et al. PHITS: Particle and heavy ion transport code system, version 2.23, JAEA-Data/Code, 2010-022. Tokai: Japan Atomic Energy Agency; 2010.
- [4] Matsuda N, Iwamoto Y, Harada M et al. Analyses of benchmark problems for the shielding design of high intensity proton accelerator facilities, JAEA-Technology, 2008-030. Tokai: Japan Atomic Energy Agency; 2008.
- [5] Titarenko Y, Batyaev V, Butko M et al. Verification of high-energy transport codes on the basis of activation data. *Phys Rev C.* 2011;84:064612.
- [6] Boudard A, Cugnon J, David J et al. New potentialities of the Liege intranuclear cascade model for reactions induced by nucleons and light charged particles. *Phys Rev C.* 2013;87:014606.
- [7] Hirayama H, Namito Y, Bielajew A et al. The EGS5 code system, SLAC-R-730 and KEK Report 2005-8. Stanford (CA) and Tsukuba: SLAC and KEK; 2005.
- [8] Noda S, Hashimoto S, Sato T et al. Improvement of photonuclear reaction model below 140 MeV in the PHITS code. *J Nucl Sci Technol.* 2015;52:57–62.
- [9] Niita K, Chiba S, Maruyama T et al. Analysis of the (N,xN') reactions by quantum molecular dynamics plus statistical decay model. *Phys Rev C.* 1995;52:2620–2635.
- [10] Ogawa T, Sato T, Hashimoto S et al. Energy-dependent fragmentation cross sections of relativistic ^{12}C . *Phys Rev C.* 2015;92:024614.
- [11] Shibata K, Iwamoto O, Nakagawa T et al. JENDL-4.0: a new library for nuclear science and engineering. *J Nucl Sci Technol.* 2012;48:1–30.
- [12] Nara Y, Otuka H, Ohnishi A et al. Relativistic nuclear collisions at 10A GeV energies from p + Be to Au + Au with the hadronic cascade model. *Phys Rev C.* 1999;61:024901.
- [13] Hashimoto S, Iwamoto O, Iwamoto Y et al. New approach for nuclear reaction model in the combination of intra-nuclear cascade and DWBA. *Nucl Data Sheets.* 2014;118:258–261.
- [14] Hashimoto S, Iwamoto O, Iwamoto Y et al. PHITS simulation of quasi-monoenergetic neutron sources from $^7\text{Li}(p,n)$ reactions. *Energy Procedia.* 2015;71:191–196.
- [15] Furihata S. Statistical analysis of light fragment production from medium energy proton-induced reactions. *Nucl Instrum Methods B.* 2000;171:251–258.
- [16] ATIMA code. Hesse; 2014. Available from: <https://web-docs.gsi.de/~weick/atima/>.
- [17] X-5 Monte Carlo Team. MCNP – a general N-particle transport code, version 5, volume I: overview and theory, LA-UR-03-1987. Los Alamos (NM): Los Alamos National Laboratory; 2003.
- [18] Abe S, Sato T. Implementation of muon interaction models in PHITS. *J Nucl Sci Technol.* 2017;54:101–110.
- [19] Leray S, Borne F, Crespin S et al. Spallation neutron production by 0.8, 1.2, and 1.6 GeV protons on various targets. *Phys Rev C.* 2002;65:044621.
- [20] Meier M, Amian W, Goulding C et al. Differential neutron production cross sections for 256-MeV protons. *Nucl Sci Eng.* 1992;110:289–298.
- [21] Ledoux X, Borne F, Boudard A et al. Spallation neutron production by 0.8, 1.2, and 1.6 GeV protons on Pb targets. *Phys Rev Lett.* 1999;82:4412–4415.
- [22] Guertin A, Marie N, Auduc S et al. Neutron and light-charged-particle productions in proton-induced reactions on ^{208}Pb at 62.9 MeV. *Eur Phys J A.* 2005;23:49–60.
- [23] J.-C. David. Spallation reactions: a successful interplay between modeling and applications. *Eur Phys J A.* 2015;51:68.

- [24] Iwamoto Y, Hagiwara M, Satoh D et al. Characterization of high-energy quasi-monoenergetic neutron energy spectra and ambient dose equivalents of 80–389 MeV ${}^7\text{Li}(p,n)$ reactions. *Nucl Instrum Methods A*. 2015;804:50–58.
- [25] Nuclear data center in JAEA. Available from: <http://www.wndc.jaea.go.jp/ftpnd/jendl/jendl40he.html>
- [26] Satoh D, Moriguchi D, Kajimoto T et al. Measurement of neutron-production double-differential cross-sections on carbon bombarded with 290-MeV/nucleon carbon and oxygen ions. *Nucl Instrum Methods A*. 2011;644:59–67.
- [27] Budzanowski A, Fidelus M, Filges D et al. Comparison of nonequilibrium processes in $p + \text{Ni}$ and $p + \text{Au}$ collisions at GeV energies. *Phys Rev C*. 2010;82:034605.
- [28] Fortsch S, Cowley A, Lawrie J et al. Continuum protons from $\text{Ni}(p, p')$ at incident energies between 100 and 200 MeV. *Phys Rev C*. 1991;43:691–700.
- [29] Cowley A, Arendse G, Koen J et al. Inclusive (p, α) reactions on ${}^{27}\text{Al}$, ${}^{59}\text{Co}$, and ${}^{197}\text{Au}$ at incident energies of 120, 160, and 200 MeV. *Phys Rev C*. 1996;54:778–783.
- [30] Villagrasa C, Boudard A, Ducret J et al. Measurement of residual nucleus cross sections and recoil energies in $p + \text{Fe}$ collisions at 300, 500, 750, 1000 and 1500 MeV. *AIP Conf Proc*. 2005;769:842–845.
- [31] Enqvist T, Wlazole W, Armbruster P et al. Isotopic yields and kinetic energies of primary residues in 1 A GeV ${}^{208}\text{Pb} + p$ reactions. *Nucl Phys A*. 2001;686:481–524.
- [32] Furihata S, Nakamura T. Calculation of nuclide productions from proton induced reactions on heavy targets with INC/GEM. *J Nucl Sci Technol Suppl*. 2002;2:758–761.
- [33] Meier M, Goulding C, Morgan G et al. Neutron yields from stopping- and near-stopping-length targets for 256-MeV protons. *Nucl Sci Eng*. 1990;104:339–363.
- [34] Robert TM, Doering RR, Galonsky A et al. Production of neutrons with protons of 22, 30, and 40 MeV in stopping targets of carbon, aluminum, copper, silver, tantalum, and lead. *Nucl Sci Eng*. 2004;147:73–82.
- [35] Watanabe Y, Kosako K, Kunieda S et al. Status of JENDL high energy file. *J Korean Phys Soc*. 2011;59:1040–1050.
- [36] Nakao N, Nakashima H, Nakamura T et al. Transmission through shields of quasi-monoenergetic neutrons generated by 43- and 68-MeV protons - I: concrete shielding experiment and calculation for practical application. *Nucl Sci Eng*. 1996;124:228–242.
- [37] Nakashima H, Nakao N, Tanaka S-I et al. Transmission through shields of quasi-monoenergetic neutrons generated by 43- and 68-MeV protons - II: iron shielding experiment and analysis for investigating calculational method and cross-section data. *Nucl Sci Eng*. 1996;124:243–257.
- [38] Hagiwara M, Iwase H, Kirihara Y et al. Benchmark experiment of neutron penetration through iron and concrete shields for hundreds-of-MeV quasi-monoenergetic neutrons - II: measurements of neutron spectrum by an organic liquid scintillator. *Nucl Technol*. 2009;168:304–309.
- [39] Yashima H, Iwase H, Hagiwara M et al. Benchmark experiment of neutron penetration through iron and concrete shields for hundreds-of-MeV quasi-monoenergetic neutrons - I: measurements of neutron spectrum by a multimoderator spectrometer. *Nucl Technol*. 2009;168:298–303.
- [40] Nakashima H. Research activities on neutronics under ASTE collaboration at AGS/BNL. *J Nucl Sci Technol Suppl*. 2002;2:1155–1166.
- [41] Nakashima H, Takada H, Kasugai Y et al. Current status of the AGS spallation target experiment. In: *Shielding Aspects of Accelerators, Targets and Irradiation Facilities-SATIF 6*; 2002 Apr 10–12; Stanford, CA. Paris: OECD-NEA Press; 2002. p. 27–36.
- [42] Matsufuji N, Fukumura A, Komori M et al. Influence of fragment reaction of relativistic heavy. *Phys Med Biol*. 2003;48:1605–1623.
- [43] Landau L. On the energy loss of first particles by ionization. *J Phys (USSR)*. 1944;8:201–205.
- [44] Vavilov P. Ionization losses of high energy heavy particles. *Soviet Phys JETP*. 1957;5:749–751.
- [45] Lynch G, Dahl O. Approximations to multiple Coulomb scattering. *Nucl Instrum Methods B*. 1991;58:6–10.
- [46] Golubev A, Kantsyrev A, Luckjashin V et al. Measurement of the energy deposition profile for ${}^{238}\text{U}$ ions with specific energy 500 and 950 MeV/u in stainless steel and copper targets. *Nucl Instrum Methods B*. 2007;263:339–344.
- [47] Rester DH, Dance WE. Thick target bremsstrahlung produced by electron bombardment of targets of Be, Sn, and Au in the energy range 0.2–2.8 MeV. *J Appl Phys*. 1970;41:2682–2692.
- [48] Faddegon BA, Ross CK, Rogers DWO. Angular distribution of bremsstrahlung from 15-MeV electrons incident on thick targets of Be, Al, and Pb. *Med Phys*. 1991;18:727–739.
- [49] Ryckbosch D, Van Hoorebeke L, Van de Vyver R et al. Determination of the absorption mechanism in photon-induced pre-equilibrium reactions. *Phys Rev C*. 1990;42:444–447.
- [50] Schumacher RA, Adams GS, Ingham DR et al. $\text{Cu}(y, p)X$ reaction at $E_y = 150$ and 300 MeV. *Phys Rev C*. 1982;25:2269–2277.
- [51] Eyss HJ, Luhrs G. Photoproduction of high-energy neutrons in thick targets by electrons in the energy range 150 to 270 MeV. *Z Physik*. 1973;262:393–412.
- [52] Sato T, Shin K, Yuasa R et al. Measurement of the neutron spectrum by the irradiation of a 2.04-GeV electron beam into thick targets. *Nucl Instrum Methods A*. 2001;463:299–308.
- [53] Werner U, Koch F, Oelgart G. Kilovolt electron energy loss distribution in Si. *J Phys D*. 1988;21:116–124.
- [54] Sempau J, Fernandez-Varea J, Acosta E et al. Experimental benchmarks of the Monte Carlo code PENELOPE. *Nucl Instrum Methods B*. 2003;207:107–123.
- [55] Shortt KR, Ross CK, Bielajew AF et al. Electron beam dose distributions near standard in homogeneities. *Phys Med Biol*. 1986;31:235–249.
- [56] Nelson WR, Liu JC, Hirayama H et al. Benchmark calculations for EGS5, SLAC-PUB-10752. Stanford (CA): SLAC; 2004; p. 1–20.
- [57] Kishida N, Murata T, Asami T et al. JENDL photonuclear data file. In: Haight RC, Chadwick MB, Kawano T et al., editors. *Proceedings of the International Conference on Nuclear Data for Science and Technology (ND2004)*; 2004 Sep 26–Oct 1; Santa Fe, NM. AIP; 2005. p. 199–202.